Novel actin filaments from *Bacillus thuringiensis* form nanotubules for plasmid DNA segregation

Shimin Jiang[a,1], Akihiro Narita[b,c,1], David Popp[a,1,2], Umesh Ghoshdastider[a,1], Lin Jie Lee[a], Ramanujam Srinivasan[d,e], Mohan K. Balasubramanian[d,f,g], Toshiro Oda[h], Fujiet Koh[a], Mårten Larsson[a,i], and Robert C. Robinson[a,j,2]

[a]Institute of Molecular and Cell Biology, Agency for Science, Technology and Research, Singapore 138673, Republic of Singapore; [b]Structural Biology Research Center and Division of Biological Sciences, Nagoya University Graduate School of Science, Structural Biology Research Center and Division of Biological Sciences, Furo-cho, Chikusa-ku, Nagoya 464-8602, Japan; [c]Japan Science and Technology Agency, PRESTO, 4-1-8 Honcho Kawaguchi, Saitama 332-0012, Japan; [d]Mechanobiology Institute, National University of Singapore, Singapore 117411, Republic of Singapore; [e]National Institute of Science, Education and Research, Bhubaneswar, Orissa 751005, India; [f]Temasek Life Sciences Laboratory, National University of Singapore, Singapore 117604, Republic of Singapore; [g]Warwick Medical School, University of Warwick, Coventry CV4 7AL, England; [h]Tokai Gakuin University, Gifu 504-8511, Japan; [i]Department of Medical Biochemistry and Microbiology, Uppsala University, SE-75123 Uppsala, Sweden; and [j]Department of Biochemistry, Yong Loo Lin School of Medicine, National University of Singapore, Singapore 117597, Republic of Singapore

Edited by Thomas D. Pollard, Yale University, New Haven, CT, and approved January 12, 2016 (received for review January 7, 2016)

Here we report the discovery of a bacterial DNA-segregating actin-like protein (*Bt*ParM) from *Bacillus thuringiensis*, which forms novel antiparallel, two-stranded, supercoiled, nonpolar helical filaments, as determined by electron microscopy. The *Bt*ParM filament features of supercoiling and forming antiparallel double-strands are unique within the actin fold superfamily, and entirely different to the straight, double-stranded, polar helical filaments of all other known ParMs and of eukaryotic F-actin. The *Bt*ParM polymers show dynamic assembly and subsequent disassembly in the presence of ATP. *Bt*ParR, the DNA-*Bt*ParM linking protein, stimulated ATP hydrolysis/phosphate release by *Bt*ParM and paired two supercoiled *Bt*ParM filaments to form a cylinder, comprised of four strands with inner and outer diameters of 57 Å and 145 Å, respectively. Thus, in this prokaryote, the actin fold has evolved to produce a filament system with comparable features to the eukaryotic chromosome-segregating microtubule.

actin | ParM | plasmid | filament | microtubule

During bacterial cell division, equal distribution of replicated plasmids to the two daughter cells ensures their stable inheritance. Type II plasmid segregation systems consist of an actin-like protein (ParM) capable of nucleotide-dependent filament formation and a centrosome-like DNA region (*parC*), which are linked by an adaptor protein ParR. The model ParCMR system is that of the *Escherichia coli* R1 plasmid (1). ParM-R1 forms actin-like double-helical straight polar filaments (2), which are paired into randomly oriented bundles. The antiparallel pairing of at least two filaments is required to push apart two R1-ParR/*parC* complexes (3). All other ParMs, which have been experimentally verified to segregate DNA, including AlfA from *Bacillus subtilis* (4) and ParM-pSK41 from *Staphylococcus aureus* (5), have also been shown by electron microscopy to form polar, double-stranded straight filaments with diameters between 80 and 90 Å, similar to eukaryotic F-actin (6).

Actins and microtubules have gained dedicated functions during evolution that vary between eukaryotes and prokaryotes. During cell division, the contractile ring in prokaryotes depends on the microtubule-like protein FtsZ, whereas this task relies on actin in eukaryotes. In contrast, DNA segregation in eukaryotes is orchestrated by microtubules, whereas in prokaryotes plasmid DNA segregation depends largely on the actin-like proteins ParMs, although Walker-type ATPase ParA (type I) systems (7) and microtubule-like TubZ (type III) systems have also been found (8). Therefore, a long-standing question has been whether a functional equivalent of the microtubule-like DNA segregating architecture, a hollow cylinder, can be found in bacteria.

Using X-ray crystallography, electron microscopy and biochemical assays, we have identified and characterized a novel DNA partitioning ParCMR system from *Bacillus thuringiensis* (*Bt*) encoded on the plasmid pBMB67 (9). The filament-forming motor protein, *Bt*ParM, proved to be entirely different from all previously studied ParMs; in contrast to the ParM-R1 model system, it formed dynamic double-stranded antiparallel supercoiled filaments with an outer diameter of 145 Å in the presence of ATP, which paired into four-stranded nanotubules in the presence of the adaptor protein *Bt*ParR or with the *Bt*ParR/*parC* complex. This finding demonstrates that some of the properties of the eukaryotic microtubule system in segregating DNA have also been probed during prokaryote evolution using the actin fold.

Results

To demonstrate that *Bt*ParM filaments assemble in an in vivo setting, GFP-*Bt*ParM was expressed and imaged in *Schizosaccharomyces pombe*. Long bundles of filaments were observed, which appeared to be relatively stable at the resolution of the fluorescence microscope. Depletion of ATP, by artificial suppression of the ATP regenerating system by placing the cells into PBS (10), caused the filaments to depolymerize. After the levels of ATP were allowed to recover, the filaments repolymerized. (Fig. 1*A*; Movie S1).

Significance

Actins and tubulins have dedicated functions that vary between eukaryotes and prokaryotes. During cell division, the prokaryotic contractile ring depends on the tubulin-like protein FtsZ, whereas this task relies on actin in eukaryotes. In contrast, microtubules orchestrate DNA segregation in eukaryotes, yet prokaryotic plasmid segregation often depends on actin-like proteins; this implies that actins and tubulins have somewhat interchangeable properties. Hence, we sought a bacterial filament that more closely resembles microtubules. Here, we report an actin from *Bacillus thuringiensis* that forms dynamic, antiparallel, two-stranded supercoiled filaments, which pair in the presence of a binding partner to form hollow cylinders. Thus, in this prokaryote, the actin fold has evolved to produce a filament system with comparable properties to the eukaryotic microtubule.

Author contributions: D.P., M.K.B., T.O., and R.C.R. designed research; S.J., A.N., D.P., U.G., and R.S. performed research; L.J.L., F.K., and M.L. contributed new reagents/analytic tools; S.J., A.N., D.P., and U.G. analyzed data; and D.P. and R.C.R. wrote the paper.

The authors declare no conflict of interest.

This article is a PNAS Direct Submission.

Freely available online through the PNAS open access option.

Data deposition: The atomic coordinates have been deposited in the Protein Data Bank, www.pdb.org (PDB ID codes 4XE7, 4XE8, 4XHO, 4XHN, and 4XHP).

[1]S.J., A.N., D.P., and U.G. contributed equally to this work.

[2]To whom correspondence may be addressed. Email: rrobinson@imcb.a-star.edu.sg or dpopp@imcb.a-star.edu.sg.

This article contains supporting information online at www.pnas.org/lookup/suppl/doi:10.1073/pnas.1600129113/-/DCSupplemental.

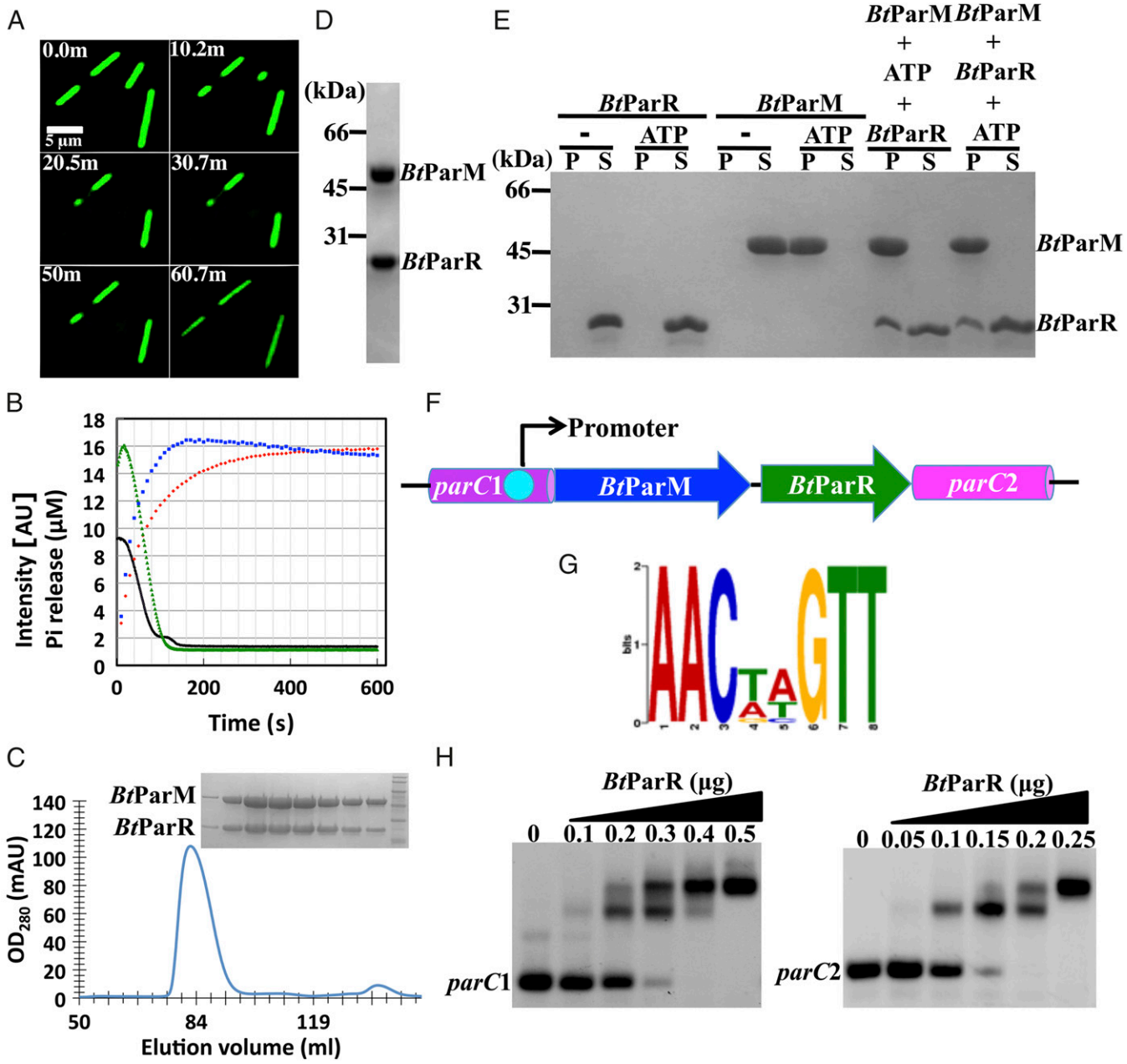

Fig. 1. (*A*) GFP-labeled *Bt*ParM expressed in *S. pombe* visualized over time. Filament bundles shortened over time on depletion of ATP, and repolymerized on restoration of ATP levels. Buffer: 40 mM Hepes, pH 7.5, 300 mM KCl, 3 mM $MgCl_2$. (*B*) Polymerization kinetics of *Bt*ParM (15 μM, green) and *Bt*ParM/ParR complex (15 μM each, black) induced by ATP (3 mM) observed by light scattering. Pi release by *Bt*ParM is shown in red and that from *Bt*ParM/ParR polymerization in blue. (*C*) *Bt*ParM/ParR complex mobility on gel filtration. (*Inset*) SDS gel of the *Bt*ParM/ParR peak. (*D*) SDS gel of the *Bt*ParM/His–ParR complex purified by nickel ion affinity chromatography. (*E*) Cosedimentation assay of *Bt*ParM and *Bt*ParR. P and S indicate the pellet and soluble fractions, respectively. (*F*) Cartoon of the ParCMR region of the pBMB67 plasmid. *parC* is separated in this system, upstream *parC1* and downstream *parC2*. (*G*) The palindromic repeats (Table S1). (*H*) In vitro EMSA gel shift analysis of the interaction of *Bt*ParR with *parC1* (200 ng) and *parC2* (200 ng).

The elongation and depolymerization phases were observed to occur at both ends of the GFP-*Bt*ParM filament bundles.

We further investigated the polymerization dynamics of *Bt*ParM in vitro by monitoring light scattering from filaments, a technique that reflects average particle size in solution. Bacterial cells are known to contain ~300 mM KCl (11), 2–3 mM $MgCl_2$ (12), and 1.5–3 mM ATP (13). Under such physiological buffer conditions, in vitro *Bt*ParM polymerization occurred above a critical concentration of 5 μM (Fig. 1*B* and Fig. S1 *A* and *B*). This value is 2× higher than found for ParM-R1 (14). ParM-R1 concentrations have been shown to be 12–14 μM in the bacterial cell (15), well above the critical concentration.

Filament formation by *Bt*ParM induced ATP hydrolysis; however, phosphate release was slower than filament assembly (Fig. 1*B*). The number of hydrolyzed ATP molecules within the polymerization–depolymerization cycle roughly equaled the number of *Bt*ParM monomers in solution, which confirms that in the *Bt*ParM system, as with other actins, ATP binding, ATP hydrolysis, and phosphate release act as a timing mechanism in orchestrating the polymerization/depolymerization cycle (16).

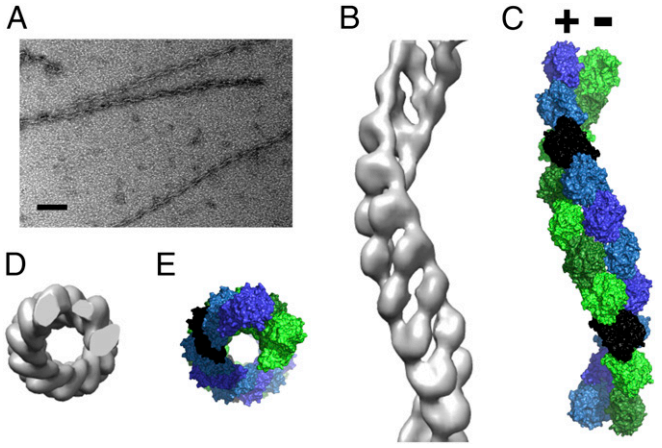

Fig. 2. (*A*) Typical electron micrograph of *Bt*ParM filaments that was used for image analysis. Note the twisted appearance. (Scale bar: 100 nm.) (*B*) A 3D electron density map of *Bt*ParM at 18.6 Å resolution (side view). (*C*) After rigid-body fitting of the monomer in its closed form into the electron density map, the antiparallel, supercoiled nature of the *Bt*ParM filament became more apparent (side view). Monomers highlighted in black illustrate the antiparallel nature of this filament. (*D* and *E*) Top views of electron density map and fitted model, respectively.

Filaments also formed from *Bt*ParM in the presence of *Bt*ParR at physiological ATP concentrations, both polymerization and depolymerization phases being slightly faster than for *Bt*ParM alone (Fig. 1*B*). In the presence of *Bt*ParR, phosphate release was faster, indicating that *Bt*ParR stimulated ATP hydrolysis and/or phosphate release, concomitant with the faster assembly–disassembly rates (Fig. 1*B*). Again, the number of hydrolyzed ATP molecules, within a polymerization–depolymerization cycle, roughly equaled the number of *Bt*ParM monomers when polymerized from the *Bt*ParM/ParR complex (Fig. 1*B*).

Quantitative gel filtration indicated that, in the absence of nucleotide, *Bt*ParR, binds strongly to the *Bt*ParM monomer in a 1:1 ratio (Fig. 1*C*). *Bt*ParM coexpressed with His-tagged *Bt*ParR was also found in a Ni^{2+}-resin pull-down assay to elute as a complex (Fig. 1*D*). A pelleting assay indicated that *Bt*ParM filaments formed in the presence of *Bt*ParR had lower amounts of bound *Bt*ParR (Fig. 1*E*), suggesting that *Bt*ParR was released during polymerization. This sedimentation assay was performed in higher than physiological ATP concentrations (10 mM), which slowed depolymerization significantly (Fig. S1*C*), allowing for filament sedimentation in a centrifuge. The *Bt*ParCMR system contains two *parC* regions (*parC1* and *parC2*) in the operon (Fig. 1*F*) with almost identical palindromic repeats (Fig. 1*G*). Electrophoretic mobility shift assays (EMSAs) for *Bt*ParR and *parC* confirmed their in vitro interaction (Fig. 1*H*; Fig. S2).

Under the electron microscope, ATP-induced polymerization of the 47.5-kDa *Bt*ParM (Fig. S3*A*) taken at the top of the polymerization curve (Fig. 1*B*) showed single filaments (Fig. 2*A*). However, the appearance of the filaments differed from ParM-R1 or F-actin polymers, in that they appeared twisted. The *Bt*ParM filaments were reconstructed following procedures successfully applied in F-actin and ParM-R1 reconstructions (14, 17). In brief, an initial 3D structure was produced by helical reconstruction (18) using eight layer lines (~54-Å resolution; Fig. S3*C*) in the EOS software package (19). This reconstructed map was used as the initial structure for the refinement steps. The filaments were treated as polar objects throughout the refinement; however, the final electron density map (Fig. S3*D*) revealed the *Bt*ParM filament to be comprised of two antiparallel strands (Fig. 2 *B* and *C*), in contrast to the polar double-stranded filaments observed for F-actin and ParM-R1 (2, 6). The *Bt*ParM monomer structure obtained by crystallography (see below) was unambiguously fitted into the 18.6-Å resolution electron density map using rigid body refinement, which clearly revealed the unique antiparallel and supercoiled geometry of this filament (Fig. S3 *B* and *D*). The outer diameter of the *Bt*ParM filament (~145 Å; Fig. 2 *D* and *E*) is substantially larger than the diameters of the non-supercoiled filaments of F-actin and ParM-R1, which are typically 80–90 Å (6, 14).

In the presence of *Bt*ParR, the filament structure, again taken at the top of the polymerization curve (Fig. 1*B*), had an entirely different appearance and somewhat resembled the projection image of a microtubule (Fig. 3*A*). A 3D helical reconstruction at 23-Å resolution (Fig. S4) revealed that the *Bt*ParM filament formed from *Bt*ParM/ParR is a four-stranded cylinder, which we refer to as a nanotubule (Fig. 3 *B* and *D*). The structure of the nanotubule involves the pairing of two antiparallel *Bt*ParM two-stranded filaments, such that each strand is antiparallel to its immediate neighbors (Fig. 3 *C* and *E*; Movie S2). No density was observed that could be attributed to ParR, suggesting that ParR is not associated at high stoichiometric ratios with the ParM nanotubules, consistent with the sedimentation studies (Fig. 1*E*).

The filament pairing mechanism seems to accelerate polymerization and ATP hydrolysis/phosphate release (Fig. 1*B*). Nanotubules assembled directly from the *Bt*ParM/ParR 1:1 complex by the addition of ATP showed an abundance of unbound *Bt*ParR (Fig. 3*A*), highlighted in Fig. S5. The *Bt*ParR appeared to form short oligomers of ~300 Å in length, which were often curved and forming half or full rings (Fig. S5). The observed average length is compatible with 10 dimers of *Bt*ParR, as proposed previously for ParCMR systems (20). In the presence of the *Bt*ParR/*parC* complex, *Bt*ParM filaments were also paired into cylinders, which additionally were often arranged in larger suprastructures consisting of rafts of ~2–10 nanotubules (Fig. S4*C*).

Several high-resolution crystal structures of *Bt*ParM were obtained (Fig. 4). To facilitate crystallization in the presence of nucleotides, mutants were designed to prevent polymerization (Tables S1 and S2). Both in the apo- and ADP-bound forms, *Bt*ParM packed into untwisted protofilaments within the crystal, which proved to be structurally relevant because the crystal contacts reproduced some of the interstrand interactions found in the left-handed EM filament model (Fig. S6). After the structure of the four protomers that define the two-stranded filament had been refined by molecular dynamics (MD) (Fig. S7; Movie S3), common interstrand

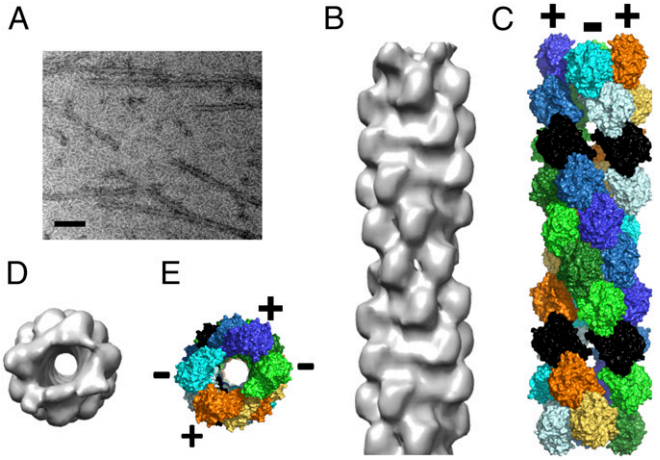

Fig. 3. (*A*) Typical electron micrograph showing *Bt*ParM filaments paired into doublets in the presence of *Bt*ParR. (Scale bar: 100 nm.) (*B*) EM reconstruction of the *Bt*ParM/ParR complex, 23 Å resolution (side view). (*C*) Model of the *Bt*ParM nanotubule after rigid-body fitting (side view). Protomers highlighted in black show the pairing of two *Bt*ParM filaments into a nanotubule. (*D* and *E*) Top views of the electron density map and the fitted model, respectively.

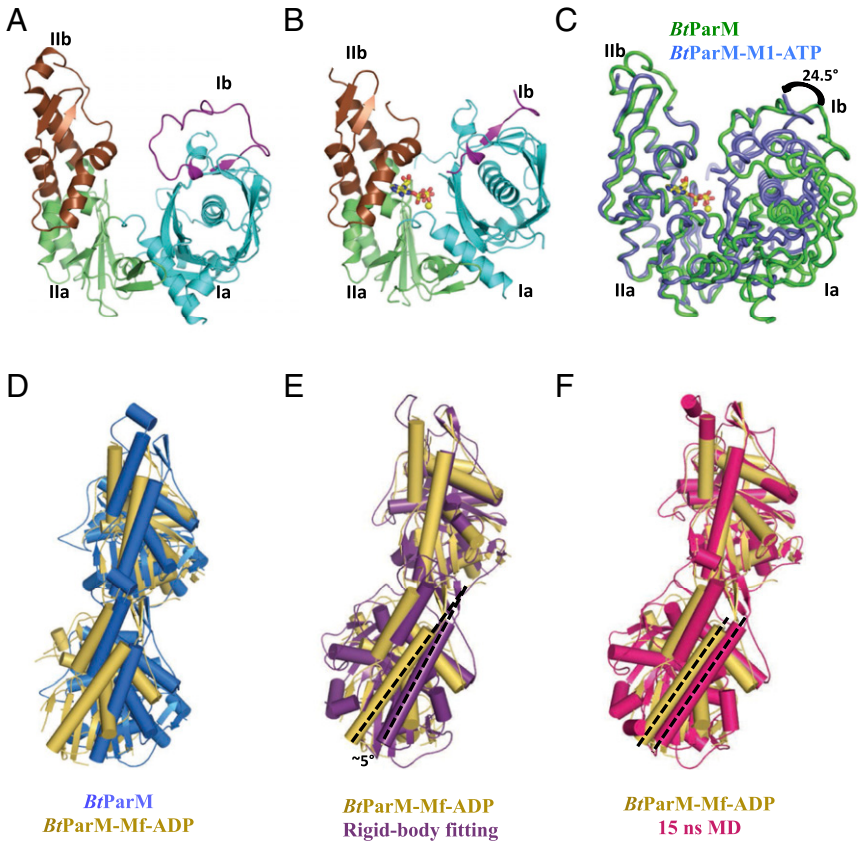

Fig. 4. (*A*) *Bt*ParM monomer X-ray structure in the open state. The four subdomains are colored: subdomain Ia (cyan), Ib (magenta), IIa (green), and IIb (brown). (*B*) *Bt*ParM structure with nucleotide ATP (sticks) and magnesium ion (yellow sphere) in the closed state. (*C*) Superposition of domain II of both *Bt*ParM open and closed states reveals that domain I undergoes a propeller-like twist from open to closed state, and subdomain Ib rotates by 24.5° toward the nucleotide-binding cleft (Movie S5). Comparison of the asymmetric unit dimer (*Bt*ParM-Mf-ADP, yellow; Fig. S8*B*) with (*D*) the protofilament in the crystal packing of apo *Bt*ParM (blue); (*E*) the rigid-body fit of the *Bt*ParM-ATP crystal structure into the EM electron density map (purple); and (*F*) the EM reconstruction after MD refinement (15 ns MD, red). In each case, the upper protomers are superimposed. The dashed black lines in the lower protomers highlight the relative orientations between the lower protomers.

filament interactions were apparent between the crystal packing and EM model; these involve Trp359, Phe360, and Asn363 of the upper portion of domain IIa and Gly330, Pro331, Lys328, and Trp329 of the lower portion of domain IIb (Fig. S6).

To determine the specificity of these intrastrand protomer interactions, a two-protomer mutant fusion strategy was adopted to disrupt the protofilament (Fig. S8), which was then studied by crystallography. In this crystal form, the asymmetric unit contains a dimer that largely reproduces the intrastrand interactions with the EM structure, yet beyond the dimeric unit the protofilament was disrupted, a testament to the functionality of this interaction (Fig. 4 *D*–*F*; Fig. S8). MD simulations of the four protomers that define the antiparallel filament proved to be stable (Movie S3), whereas the eight protomers that define the nanotubule were unstable (Movie S4). This finding is in line with *Bt*ParR being necessary to initiate the bringing of two filaments together to form the nanotubule, a likely requirement for plasmid segregation.

Without nucleotide, the structure of the *Bt*ParM monomer adopted an open conformation, which closed on binding the nucleotide and Mg^{2+} (Fig. 4 *A*–*C*). This conformational change involves a propeller-like twist from the open to the closed state and a relative change of angle between the two domains of 24.5°, similar to observations for ParM-R1 (Fig. 4 *A*–*C*; Movie S5) (3). As with ParM-R1, atomic structures of *Bt*ParM with bound ATP or ADP were almost identical and did not reveal the mechanism of ATP hydrolysis (Fig. 3*B*; Fig. S9). In ParM-R1, Glu148 has been speculated to be involved in hydrolysis (3). Interestingly, the corresponding residue in *Bt*ParM (Glu201) is at virtually the same position as in ParM-R1 when comparing the apo structures. In the presence of nucleotide, Glu148 in ParM-R1 only changes its side-chain position, whereas Glu201 in *Bt*ParM moves away (12 Å) from its apo position (Fig. S10). Therefore, we speculate that Glu201 in *Bt*ParM acts as a molecular switch triggering ATP hydrolysis.

ParM-R1 polymerizes with a large variety of nucleotides, including ATP, GTP, AMPPNP, and GMPPNP (14), whereas *Bt*ParM only formed filaments in the presence of ATP. In ParM-R1, the purine of the GDP and GMPPNP is involved in H-bonding with Glu284 but not with ADP or AMPPNP (3). Glu284 is not present in *Bt*ParM and may explain the selectivity toward ATP (Fig. S11). The ATP binding site, which is preserved between all actin-like proteins, acts as an ATP hydrolysis and phosphate release controlled conformational switch that is activated by polymerization (21). The ATP switch acts as a timing mechanism to coordinate polymerization and depolymerization (Fig. 1*B*) (16). *Bt*ParM binding to energy-rich ATP causes the nucleotide binding cleft to narrow, allowing the monomer to adopt the polymerization-competent conformation (Fig. 4 *A*–*C*). Filament formation stimulates ATP hydrolysis (Fig. 1*B*), and its transformation into ADP leads to filament destabilization. Thus, we propose that the ADP-bound *Bt*ParM within a filament is primed for disintegration, whereas the ATP-bound *Bt*ParM monomer results in a conformational primed for association.

*Bt*ParM filaments are highly negatively charged with an effective charge density of 7.4 e/nm (Fig. S12) in the presence of 300 mM salt, typical for bacterial cells. *Bt*ParM filaments alone do not self-assemble into nanotubules, but require the binding of *Bt*ParR to

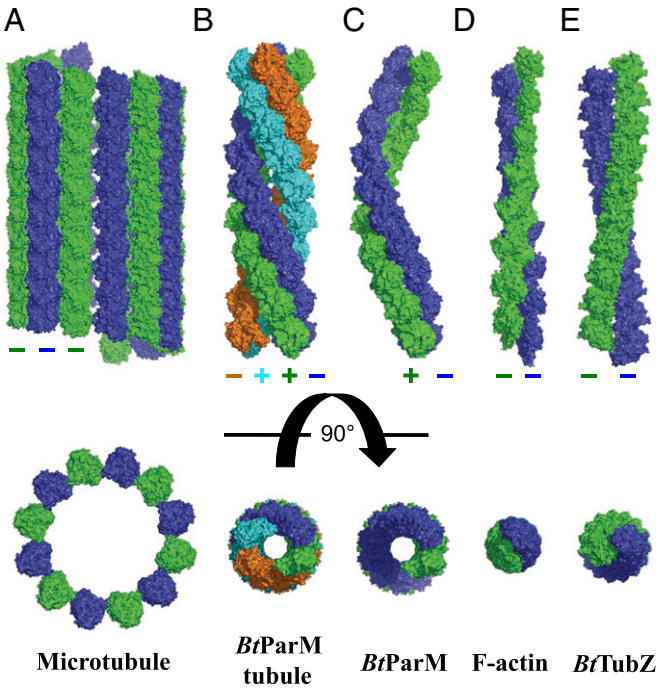

Fig. 5. Comparison of actin-like and tubulin-like filament structures. (*A*) Mammalian microtubule. (*B*) *B. thuringiensis* actin-like *Bt*ParM nanotubule. (*C*) *B. thuringiensis* actin-like *Bt*ParM filament. (*D*) Mammalian F-actin. (*E*) *B. thuringiensis* tubulin-like TubZ. The filament systems are depicted with 10 protomers in each strand, with the exception of F-actin, which has eight. (*Upper*) Side views. (*Lower*) Top views.

pair filaments into a nanotubule. To form the nanotubule, *parC* was not a requirement under the conditions tested. Pairing two *Bt*ParM filaments into a cylinder will increase the rigidity of the polymerizing motor. Clamping two highly negatively charged filaments into a cylinder will store energy, which may be relevant for both nanotubule dynamics and plasmid segregation. However, determination of the mechanism of segregation will likely require studies in the host organism.

Discussion

Microtubules form hollow cylinders with 230 Å outer and 180 Å inner diameters consisting of 12–14 parallel protofilaments (Fig. 5). In comparison, the *Bt*ParM nanotubule from *B. thuringiensis* consists of four antiparallel filament strands with dimensions 145 Å and 57 Å (Fig. 5). Tubulin-like DNA segregating proteins are rare in bacteria and, to date, they have not been shown to form a microtubule-like structure (8). Interestingly, one example, TubZ, a treadmilling polymer, which segregates the pBtoxis plasmid, also from *B. thuringiensis*, forms straight two- or four-stranded polar filaments in vitro dependent on nucleotide (22) and does not form a microtubule-like filament (Fig. 5). In conclusion, we show that the bacterial actin *Bt*ParM, which segregates plasmid DNA, forms dynamic nanotubules, properties that largely resemble those of eukaryotic microtubules in segregating chromosomes. These data suggest that the ParM-R1 model system (3) and the *Bt*ParCMR system are likely to be just two of many type II plasmid segregation mechanisms operating in bacteria.

Materials and Methods

Complete materials and methods are reported in *SI Materials and Methods*. Briefly, proteins were generally obtained by gene synthesis as N-terminal His-tagged constructs followed by expression in *E. coli* and purified by Ni^{2+}-affinity chromatography, ion exchange chromatography, and/or gel filtration. The crystal structure of the *Bt*ParM monomer was initially elucidated using data collected from selenium methionine *Bt*ParM crystals (I24; Diamond Light Source) using the SAD method. Subsequent structures were solved by molecular replacement using this initial structure as the search model from data collected at beamline BL13B1 at the National Synchrotron Radiation Research Center (NSRRC) in Taiwan. Negative-stain electron micrographs were collected on a cooled 4K CCD camera mounted on either a JEOL 1400 or a JEOL 2200 electron microscope operated at 100–200 keV with nominal magnifications of 40,000. Fourier transforms and 3D reconstructions were obtained using the EOS software package (19), and structures were fitted to the electron density using rigid body refinement followed by MD.

Sedimentation studies were carried out at high levels of ATP [40 mM Hepes (pH 7.5), 350 mM KCl, 5 mM $MgCl_2$, and 10 mM ATP] to prevent depolymerization. In vitro assembly and disassembly was followed by light (600 nm) scattering monitored at 90°. Release of inorganic phosphate was measured using the Phosphate Assay Kit (E-6646; Molecular Probes).

ACKNOWLEDGMENTS. We thank Jonathan Grimes for help with X-ray data collection and the Joint Centre for Structural Biology (Singapore) for providing research facilities, supported by grants from Nanyang Technological University and the Biomedical Research Council of the Agency for Science, Technology and Research (A*STAR). Parts of this study were carried out on beamline BL13B1 at the National Synchrotron Radiation Research Center (Taiwan) and I24 at the Diamond Light Source (Great Britain) under proposal MX8423. This work was supported by A*STAR in Singapore and Joint Council Office Grant Project 12302FG012 (to S.J., D.P., and R.C.R.); the Mechanobiology Institute and Temasek Life Science Institute (Singapore) (R.S. and M.K.B.); and the Japan Society for the Promotion of Science (JSPS) KAKENHI Grant 14431234 (to A.N.).

1. Gerdes K, Howard M, Szardenings F (2010) Pushing and pulling in prokaryotic DNA segregation. *Cell* 141(6):927–942.
2. Bharat TA, Murshudov GN, Sachse C, Löwe J (2015) Structures of actin-like ParM filaments show architecture of plasmid-segregating spindles. *Nature* 523(7558):106–110.
3. Gayathri P, et al. (2012) A bipolar spindle of antiparallel ParM filaments drives bacterial plasmid segregation. *Science* 338(6112):1334–1337.
4. Polka JK, Kollman JM, Mullins RD (2014) Accessory factors promote AlfA-dependent plasmid segregation by regulating filament nucleation, disassembly, and bundling. *Proc Natl Acad Sci USA* 111(6):2176–2181.
5. Popp D, et al. (2010) Structure and filament dynamics of the pSK41 actin-like ParM protein: Implications for plasmid DNA segregation. *J Biol Chem* 285(13):10130–10140.
6. Holmes KC, Popp D, Gebhard W, Kabsch W (1990) Atomic model of the actin filament. *Nature* 347(6288):44–49.
7. Szardenings F, Guymer D, Gerdes K (2011) ParA ATPases can move and position DNA and subcellular structures. *Curr Opin Microbiol* 14(6):712–718.
8. Aylett CH, Wang Q, Michie KA, Amos LA, Löwe J (2010) Filament structure of bacterial tubulin homologue TubZ. *Proc Natl Acad Sci USA* 107(46):19766–19771.
9. Chao L, et al. (2007) Complete nucleotide sequence of pBMB67, a 67-kb plasmid from *Bacillus thuringiensis* strain YBT-1520. *Plasmid* 57(1):44–54.
10. Saitoh S, Yanagida M (2014) Does a shift to limited glucose activate checkpoint control in fission yeast? *FEBS Lett* 588(15):2373–2378.
11. Cayley S, Lewis BA, Guttman HJ, Record MT, Jr (1991) Characterization of the cytoplasm of *Escherichia coli* K-12 as a function of external osmolarity. Implications for protein-DNA interactions in vivo. *J Mol Biol* 222(2):281–300.
12. Alatossava T, Jütte H, Kuhn A, Kellenberger E (1985) Manipulation of intracellular magnesium content in polymyxin B nonapeptide-sensitized *Escherichia coli* by ionophore A23187. *J Bacteriol* 162(1):413–419.
13. Yaginuma H, et al. (2014) Diversity in ATP concentrations in a single bacterial cell population revealed by quantitative single-cell imaging. *Sci Rep* 4:6522.
14. Popp D, et al. (2008) Molecular structure of the ParM polymer and the mechanism leading to its nucleotide-driven dynamic instability. *EMBO J* 27(3):570–579.
15. Møller-Jensen J, Jensen RB, Löwe J, Gerdes K (2002) Prokaryotic DNA segregation by an actin-like filament. *EMBO J* 21(12):3119–3127.
16. Ghoshdastider U, Jiang S, Popp D, Robinson RC (2015) In search of the primordial actin filament. *Proc Natl Acad Sci USA* 112(30):9150–9151.
17. Narita A, Maéda Y (2007) Molecular determination by electron microscopy of the actin filament end structure. *J Mol Biol* 365(2):480–501.
18. Stewart M (1988) Computer image processing of electron micrographs of biological structures with helical symmetry. *J Electron Microsc Tech* 9(4):325–358.
19. Yasunaga T, Wakabayashi T (1996) Extensible and object-oriented system Eos supplies a new environment for image analysis of electron micrographs of macromolecules. *J Struct Biol* 116(1):155–160.
20. Schumacher MA, et al. (2007) Segrosome structure revealed by a complex of ParR with centromere DNA. *Nature* 450(7173):1268–1271.
21. Gunning PW, Ghoshdastider U, Whitaker S, Popp D, Robinson RC (2015) The evolution of compositionally and functionally distinct actin filaments. *J Cell Sci* 128(11):2009–2019.
22. Montabana EA, Agard DA (2014) Bacterial tubulin TubZ-Bt transitions between a two-stranded intermediate and a four-stranded filament upon GTP hydrolysis. *Proc Natl Acad Sci USA* 111(9):3407–3412.

23. Chumnarnsilpa S, et al. (2009) The crystal structure of the C-terminus of adseverin reveals the actin-binding interface. *Proc Natl Acad Sci USA* 106(33):13719–13724.
24. Adams PD, et al. (2010) PHENIX: A comprehensive Python-based system for macromolecular structure solution. *Acta Crystallogr D Biol Crystallogr* 66(Pt 2):213–221.
25. Emsley P, Cowtan K (2004) Coot: Model-building tools for molecular graphics. *Acta Crystallogr D Biol Crystallogr* 60(Pt 12 Pt 1):2126–2132.
26. Chen VB, et al. (2010) MolProbity: All-atom structure validation for macromolecular crystallography. *Acta Crystallogr D Biol Crystallogr* 66(Pt 1):12–21.
27. Zerby D, Lieberman PM (1997) Functional analysis of TFIID-activator interaction by magnesium-agarose gel electrophoresis. *Methods* 12(3):217–223.
28. Srinivasan R, Mishra M, Wu L, Yin Z, Balasubramanian MK (2008) The bacterial cell division protein FtsZ assembles into cytoplasmic rings in fission yeast. *Genes Dev* 22(13):1741–1746.
29. Webb MR (1992) A continuous spectrophotometric assay for inorganic phosphate and for measuring phosphate release kinetics in biological systems. *Proc Natl Acad Sci USA* 89(11):4884–4887.
30. Zhao FQ, Craig R (2003) Capturing time-resolved changes in molecular structure by negative staining. *J Struct Biol* 141(1):43–52.
31. Popp D, et al. (2012) Novel actin-like filament structure from *Clostridium tetani*. *J Biol Chem* 287(25):21121–21129.
32. van Heel M, Schatz M (2005) Fourier shell correlation threshold criteria. *J Struct Biol* 151(3):250–262.
33. Wriggers W, Birmanns S (2001) Using situs for flexible and rigid-body fitting of multiresolution single-molecule data. *J Struct Biol* 133(2-3):193–202.
34. Brooks BR, et al. (1983) CHARMM: A program for macromolecular energy, minimization, and dynamics calculations. *J Comput Chem* 4:187–217.
35. Jorgensen WL, Chandrasekhar J, Madura JD, Impey RW, Klein ML (1983) Comparison of simple potential functions for simulating liquid water. *J Chem Phys* 79:926–935.
36. Pronk S, et al. (2013) GROMACS 4.5: A high-throughput and highly parallel open source molecular simulation toolkit. *Bioinformatics* 29(7):845–854.
37. Lindorff-Larsen K, et al. (2010) Improved side-chain torsion potentials for the Amber ff99SB protein force field. *Proteins* 78(8):1950–1958.
38. van der Spoel D, et al. (2010) Gromacs user manual version 4.5.4. Available at gromacs.org/.
39. Bussi G, Donadio D, Parrinello M (2007) Canonical sampling through velocity rescaling. *J Chem Phys* 126(1):014101.
40. Parrinello M (1981) Polymorphic transitions in single crystals: A new molecular dynamics method. *J Appl Phys* 52:7182–7190.
41. Essmann U, et al. (1995) A smooth particle mesh Ewald method. *J Chem Phys* 103: 8577–8593.
42. Hess B (2008) P-LINCS: A parallel linear constraint solver for molecular simulation. *J Chem Theory Comput* 4(1):116–122.
43. Delano W (2012). The PyMOL Molecular Graphics System, Version 1.5. Available at www.pymol.org.
44. Hunter JD (2007) Matplotlib: A 2D graphics environment. *Comput Sci Eng* 9:90–95.